Multiscale analysis of water vapor diffusion in low density fiberboard: implications as a building material

Patrick Perré, Romain Rémond, Giana Almeida

Multiscale analysis of water vapor diffusion in low density fiberboard: implications as a building material.

Patrick Perré[a,b,*], Romain Rémond[c], Giana Almeida[d]

[a] *LGPM, CentraleSupélec, Centre Européen de Biotechnologie et de Bioéconomie (CEBB), 3 rue des Rouges Terres, 51 110 Pomacle, France*
[b] *LGPM, CentraleSupélec, Université Paris-Saclay, 3 rue Joliot Curie, F-91 190 Gif-sur-Yvette, France*
[c] *Université de Lorraine, LERMAB, ENSTIB, Epinal, France*
[d] *Université Paris-Saclay, INRAE, AgroParisTech, UMR SayFood, 91300, Massy, France*

Abstract

This work is devoted to diffusion mechanisms in low-density fiberboard ($255\,kg.m^{-3}$). Experiments were performed under unsteady state conditions (relative humidity step from 37% to 71%) with different thicknesses (half thickness ranging from $1\,mm$ to $20\,mm$). The mass diffusivity was determined by inverse analysis from the experimental moisture content evolution, using a comprehensive macroscopic model of coupled heat and mass transfer. A clear failure of Fickian's law becomes evident regarding the effect of thickness. A dual-scale model, based on the concept of distributed microstructure models with coupled heat and mass transfer at both scales, was used to simulate the experiments. The large number of dual-scale simulations proposed in this work were also analyzed by the inverse method. These dual-scale simulation results were successfully confronted to the experiment. The good fit with the experimental data is obtained for a diffusivity of the microscopic phase (the storage phase) equal to $1.10^{-13}\,m^2.s^{-1}$ for a fiber radius of $20\,\mu m$. As the main recommendation, we advise that the dual scale effect can be neglected for this kind of fiberboard for a total thickness larger than some centimeters, depending on the panel density. This also means that this effect must be considered in material characterization or when capturing the buffering effect of the surface layers of the envelope.

Keywords: building materials, moisture buffering effect, diffusion, dual-scale, fading memory, simulation, experiment.

Nomenclature

Greek Symbols

ϵ	Volume fraction	-
μ	Viscosity	$\mathrm{Pa \cdot s}$
Φ	Porosity	-
ρ	Density	$\mathrm{kg/m^3}$
τ	Time constant	s

Roman Symbols

$\boldsymbol{n}$	Normal unit vector	-

*Corresponding author
Email address: patrick.perre@centralesupelec.fr (Patrick Perré)

	ℓ	Half-sample thickness	m
	c_p	Heat capacity	$\mathrm{J/(K \cdot m^3)}$
	D	Diffusion coefficient	$\mathrm{m^2/s}$
	f	Dimensionless mass diffusivity	-
	h	Specific enthalpy	$\mathrm{J/(K \cdot kg)}$
	h_h	Heat transfer coefficient	$\mathrm{W/(K \cdot m^2)}$
	h_m	Mass transfer coefficient	m/s
	K	Permeability	$\mathrm{m^2}$
	L_v	Latent heat of vaporization	J/kg
	m	Mass	kg
	MC	Moisture content, dry basis	-
	P	Pressure	Pa
	Q_h	Heat source (dual scale)	$\mathrm{W/m^3}$
	q_h	Flux density of heat	$\mathrm{W/m^2}$
	Q_v	Vapor source (dual-scale)	$\mathrm{kg/(s \cdot m^3)}$
	q_v	Flux density of vapor	$\mathrm{kg/(s \cdot m^2)}$
	R	Gas constant	$8.314\ \mathrm{J/(K \cdot mol)}$
	r	Radius of the microscopic fiber	m
	RH	relative humidity	-
	S	Surface area	$\mathrm{m^2}$
	T	Temperature	°C
	t	Time	s
	V	Volume	$\mathrm{m^3}$
	v	Velocity	m/s
	X	Moisture content (dry basis)	-

Subscripts

a	Air
atm	Atmospheric value
d	Dry bulb
eff	Effective value at the macroscopic scale
eq	Equilibrium
f	Fiber
g	Gaseous
h	Heat
m	Mass
mac	Macroscopic

s	Solid
v	Water vapor
w	Wet bulb or liquid water

Superscripts

$\overline{\psi}$	averaged of variable ψ over the REV
γ	Macroscopic phase (conductive phase of the dual-scale formulation)
σ	Microscopic phase (storage phase of the dual-scale formulation)

Other Symbols

∇	Gradient
$\nabla\cdot$	Divergence
∇_x	Macroscopic gradient (dual-scale formulation)
∇_y	Microscopic gradient(dual-scale formulation)

1. Introduction

Bio-based materials are increasingly used in construction thanks to their good mechanical and thermal performance and reduced ecological footprint. In the meantime, increasing thermal performance standards of buildings require efficient simulation tools together with relevant and accurate material characterization (Crawley et al., 2001; Woloszyn and Rode, 2008; Delgado et al., 2010). Due to the latent heat of water vaporization, accounting for the coupling between heat and mass transfer is mandatory in building energy simulation (BES) models, namely when highly hyroscopic materials are used. This need has resulted in a strong demand for mass transfer characterization, as we have to keep in mind that the so-called moisture buffering effect depends on both equilibrium (sorption isotherms) and mass transfer (mass diffusivity) (Künzel et al., 2005; Jacques et al., 2015). More subtle effects that affect the moisture buffering capacity must also be considered. For example, the dependence of sorption behavior on the hydric history of the product (Downes and Mackay, 1958; Christensen, 1967). This sorption hysteresis affects the energy demand of a building (Kwiatkowski et al., 2011) and must be considered in BES models (Frandsen et al., 2007; Merakeb et al., 2009; Rémond et al., 2018). Similarly, non-Fickian behaviors of bound water diffusion in hygroscopic materials have been reported. This is revealed, for example, by a slow shift in moisture content during the relative humidity (RH) plateau after a sudden change (Lelievre et al., 2014). Due to these facts, the assessment of the moisture buffering effect in the building envelope remains difficult, as it depends on the moisture load (Ge et al., 2014). In addition, it also means that the material characterization must be carried out in a transient state, as a steady-state method would be blind to the effects of a fading memory.

Low-density fiberboard (LDF) offers good thermal and acoustic insulation for housing construction. It also has a good moisture buffering capacity when exposed to changing conditions, which is good for both the outer layer of the building (summer comfort) and the health of the indoor air. However, these materials accumulate all the above-mentioned behaviors. At first, the diffusion coefficient measured under steady-state conditions (cup method) has a value different from the one obtained under unsteady-state conditions (Rémond and Almeida, 2011), which supports the need for characterization in transient state.

In addition, the parameter obtained in transient state depends on the experimental information used (local RH or moisture content) (Busser et al., 2018). As additional proof, the diffusivity value identified for fiberboard using the RH value at the back face of the sample is greater than that of the unit, which is non-physical, when using a classical macroscopic formulation of coupled transfer (Perré et al., 2015; Perré, 2015). A last but important topic: among the several time constants involved in the transient state, some depend on the macroscopic configuration, and others are tied to microscopic effects. Therefore, the balance between these time constants depends on the material dimensions, which raises the question of the relevance of transferring the laboratory measurements to the building level. The physics surrounding these deviations from Fickian behavior are nowadays well-documented (Challansonnex et al., 2019; Perré, 2019). Indeed, during transient sorption (unsteady-state conditions), the water molecules penetrate the fibers. An intrinsic coupling arises between the vapor flow through the connected void structure and the diffusion of bound water inside the fibers. The macroscopic behavior results from the relative importance of these simultaneous mechanisms. In such dual-scale effects, the macroscopic formulation must be revisited as soon as the microscopic time scale has an order of magnitude similar to or greater than the macroscopic one. In such cases, the classical macroscopic formulation fails due to the absence of local thermodynamic equilibrium (Krabbenhoft and Damkilde, 2004; Nyman et al., 2006; Silva et al., 2009; Perré, 2010). This paper proposes a full set of experimental and modeling results to rigorously address this question and propose recommendations for the characterization of such materials and their proper consideration in building simulation (Fig. 1). A full data set of transient diffusion in fiberboard (1) is analyzed using a comprehensive macroscopic model of coupled heat and mass transfer in porous media (2). This database reveals a failure of the macroscopic law of diffusion: non-Fickian behavior is evidenced (3). To explain this discrepancy, a comprehensive dual-scale model is used to generate a simulation database (4). The macroscopic behavior of these simulations was also analyzed using the same macroscopic model (2). The comparison of experimental data and dual-scale simulations allowed us to get consistent results (5) and to draw the following statements (6):

- To confirm that the non-Fickian behavior is due to the dual-scale effect,
- To propose microscopic behavior (combination of diffusivity and size) able to predict the experimental results,
- To draw practical rules when using low-density hygroscopic materials in buildings.

2. Materials and methods

2.1. Sampling

Samples used in the present study come from a low-density wood fiberboard (SteicoUniversal, Steico, Brumath, France, $255\,kg.m^{-3}$) cut perpendicularly to the board, hence tested along the board thickness. Different sample thicknesses were tested to study their effect on diffusivity behavior. All thicknesses come from a panel with an initial thickness of 24 mm. The thickness reduction was carried out using a planer. For small thickness values ($2\,mm$ and $4\,mm$, later designed as $1\,mm$ and $2\,mm$ of half-thickness), cylindrical samples of $18\,mm$ in diameter were carefully prepared and coated by applying epoxy resin on their

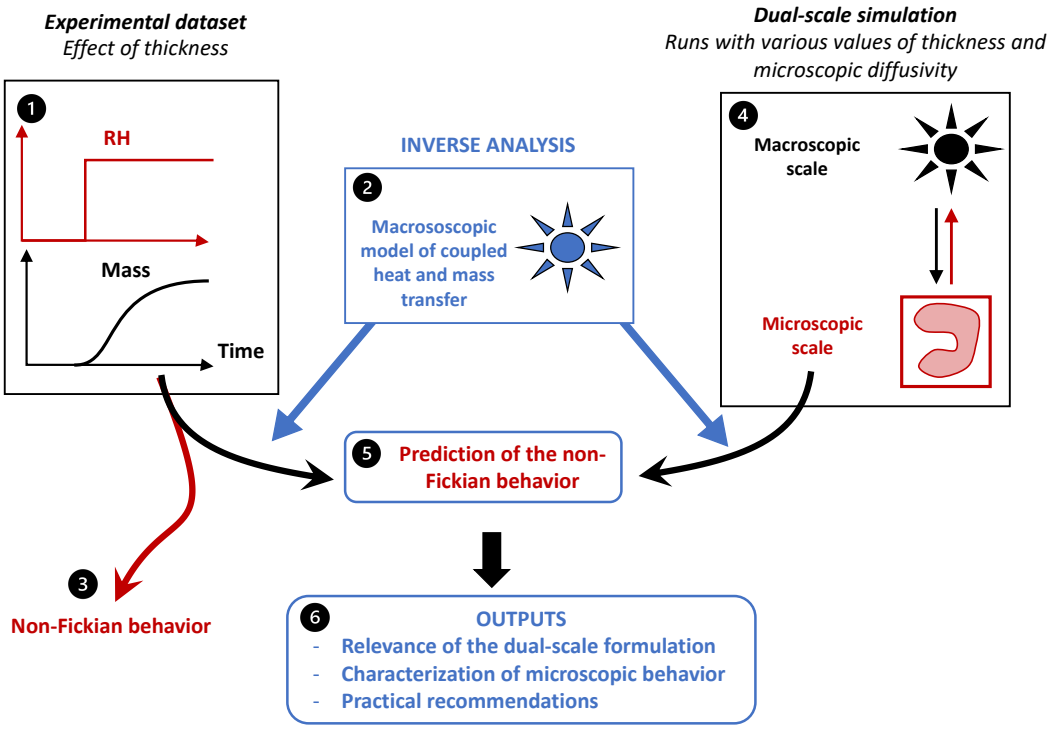

Figure 1: Structure of this work.

lateral faces. For large half-thickness values ($5\,mm$ to $24\,mm$), much larger samples (rectangles of $15 \times 20\,cm^2$) were prepared to reduce the importance of 2-D thermal transfer at lateral faces. The edges of the samples were insulated by applying an aluminum foil previously coated with a thin layer of epoxy resin. Applying the resin to the foil instead of the sample itself limits the penetration of the resin into the porous material. As the proportion of resin mass to fibers mass is not negligible for the $18\,mm$-diameter samples, uncoated samples were also tested. To obtain large half-thickness values, some of these samples were insulated from mass transfer on one face to obtain an asymmetrical configuration. This aluminum foil was applied with the same method used for the lateral faces, ensuring perfect mass transfer insulation but allowing heat transfer.

2.2. Experimental devices

For the large samples ($10\,mm$ of total thickness and above), the tests were performed using twin climatic chambers connected by an airlock designed for a rapid passage of the sample from one chamber to the other. These climatic chambers were designed to maintain a constant relative humidity over a long period of time. They consist of two volumes: the chamber itself and a lower volume with a bath containing distilled water set at the desired dew point temperature by a chiller. A fan ensures a forced airflow over the water bath and between the two volumes. The doors have two manual accesses closed with diaphragms that allow the samples to be weighed without perturbing the chamber conditions. The dry and wet bulb temperatures are recorder and subsequently used as input values for the inverse analysis. A detailed description of this device may be found in Agoua et al. (2001). To determine the diffusivity in a unsteady state, samples are maintained inside chamber

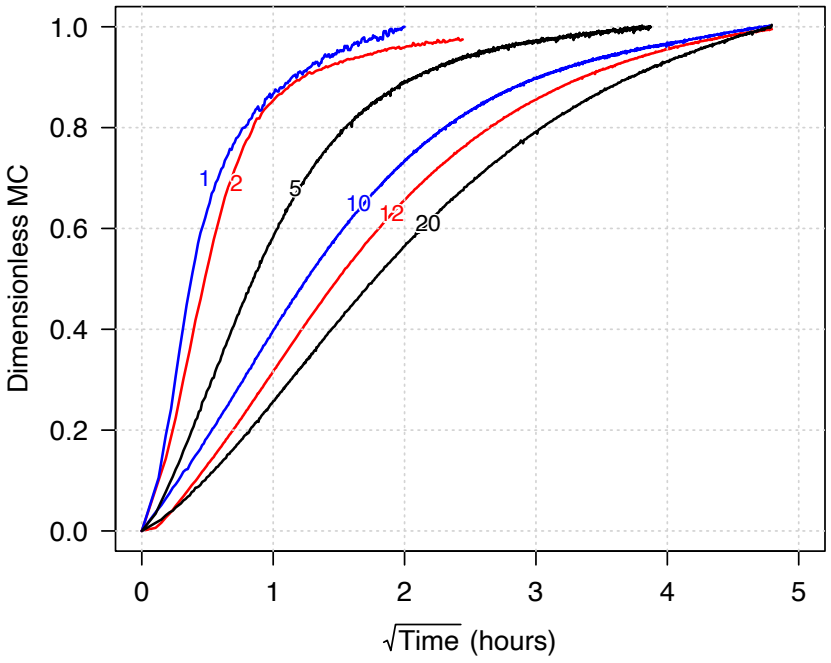

Figure 2: Raw experimental data: dimensionless mass increase versus the square root of time for six different values of half-thickness (1, 2, 5, 10, 12 and 20 mm).

1 until equilibrium. Then, the sample is passed through the airlock into chamber 2 and put on a digital balance ($\pm 0.0001\,g$) for continuous mass recording over 24 hours. Manual weighting completes the mass collection over longer periods. This allows the balance to be available for a new sample for the next 24 hours. The following conditions were used in this work:

- Climatic chamber 1: Temperature = 35^oC and dew point = 18^oC (RH = 37%);
- Climatic chamber 2: Temperature = 35^oC and dew point = 29^oC (RH = 71%).

For thinner samples (2 and 4 mm), measurements were performed in a device based on a magnetic suspension balance (Rubotherm, full load of 25 g; resolution of 0.01 mg). The balance and the electromagnet are completely disconnected from the testing chamber, avoiding cold points where condensation could occur. The magnetic suspension also permits a regular taring of the balance, thus avoiding any drift. The sample is hung on a hook fixed to the lower part of the electromagnet. The temperature is controlled by a thermostat that circulates water around the coupling housing and a double-walled jacket enclosing the testing cell. The relative humidity is set by a moist air generator (proUmid MHG32). The experimental data (mass, temperature, relative humidity) are recorded every minute. A step-wise variation of RH was applied during the tests at constant temperature (35°C): 37% RH for 48 hours; and then 71% RH for 48 hours. More details about this device can be found in (Perré et al., 2007a). Figure 2 depicts dimensionless experimental results obtained in transient diffusion tests of fibrous panels of different thicknesses. As expected, the characteristic diffusion time increases with thickness.

2.3. Inverse analysis of diffusivity

After the sudden increase in relative humidity, water vapor condenses on the front of the sample, leading to an strong coupling between heat and mass transfer. By releasing the latent heat of vaporization, this moisture flux heats the surface and, eventually, the whole sample. Because of this temperature increase, the vapor pressure at the surface increases as well as the saturated vapor pressure increases rapidly with temperature. The primary effect of this change in surface vapor pressure is to reduce the external driving force, which slows down the process. This coupling plays also an important role in the balance between external and internal resistances to transfer, which cannot be considered using either the thermal or mass Biot numbers. Instead, a dimensionless number accounting for the coupling, the drying intensity number, should be used (Perré, 2015). Without coupling, which can be simulated by setting the latent heat of vaporization equal to zero in the model, the data analysis would significantly underestimate the diffusion coefficient, up to a two-fold reduction for insulating hygroscopic materials (Perre et al., 2019). Similarly, the heat transfer on the mass-insulated face of asymmetrical samples must be considered in the simulation, as explained in the previous reference. This is why a comprehensive physical formulation was used in the present work: basically, the same set of equations as in references Perré and Turner (1999); Perré et al. (2007b).

In this model water exists in three different forms: liquid, vapor and bound water. However, for the sake of simplification, all liquid water contributions have been discarded in the present work as the sample remains inside the hygroscopic domain. Similarly, considering the particular morphology of the material, one can assume that mass transfer occurs mainly as water vapor diffusion in the gaseous phase. Thus, the transport terms of bound water have been discarded. The simplified transport equations, already presented are detailed in appendix A. Finally, the effective diffusivity is expressed as $\boldsymbol{f}$, a dimensionless proportion of the binary diffusivity of vapor in air: $\boldsymbol{D}_{eff} = \boldsymbol{f}\boldsymbol{D}_v$, where $\boldsymbol{f}$ is a dimensionless diffusivity tensor. $\boldsymbol{f}$ ranges between 0 (impervious material) and 1 (same diffusivity as the air at rest). Along one given direction, $f = 1/\mu$, where μ is the *vapor resistance ratio* used for building materials.

The diffusivity is determined by inverse analysis using a computational solution of the above set of equations. To do that, the known sample characteristics (thickness, density, porosity, dry mass, etc.), the estimated values of unknown parameters (diffusion coefficient, initial moisture content, tare) and the chamber conditions recorded throughout the test (temperature and relative humidity versus time) are supplied to the comprehensive model to simulated the sample behavior.

The external heat and mass transfer coefficients, h_h and h_m were set in the model, rather than identified, as internal and external resistances are not independent.
At first, the mass transfer coefficient h_m was defined as a function of h_h using the analogy between heat and mass transfer assuming the Lewis number to be equal to unity (Welty et al., 2009):

$$h_m = \frac{h_h}{\rho_g c_{pg}}, \tag{1}$$

The heat transfer coefficient h_h is solely controlled by the boundary layer around the sample. This is done during a drying test using a sample of similar geometry but likely to

present a constant drying rate period (CRP). During the CRP, the sample temperature is at the wet bulb temperature T_w, uniform in space and constant in time. No conductive heat flux exists. Consequently, the heat flux q_h supplied to the sample through the external heat transfer is entirely devoted to the latent heat of vaporisation required to ensure the drying rate q_v determined by the time-evolution of the sample mass:

$$L_v q_v = q_h = S h_h (T_d - T_w), \tag{2}$$

where L_v the latent heat of vaporization of water, q_v is the drying rate ($kg.m^{-2}.s^{-1}$) as determined by the time evolution of sample mass versus during the CDR period, S is the exchange surface area, T_w is the wet bulb temperature and T_d is the dry bulb temperature.

The sample size has a direct effect on the thickness of the boundary layer : h_h might therefore be surprisingly high at low velocity for small samples. Depending on the conditions, h_h values ranging from 15 to 31 $W{\cdot}\mathrm{m}^{-2}{\cdot}\mathrm{K}^{-1}$ were determined experimentally in different experimental devices (Perré and May, 2007; Colin et al., 2016; Challansonnex et al., 2019). In the present work, we used the value of 20.5 $W{\cdot}\mathrm{m}^{-2}{\cdot}\mathrm{K}^{-1}$ for small samples, as determined from CDR in the magnetic suspension balance (Challansonnex et al., 2019) and a value of 25 $W{\cdot}\mathrm{m}^{-2}{\cdot}\mathrm{K}^{-1}$ for the large samples tested in a climatic chamber with a much higher air velocity.

For the inverse procedure, the very fast 1-D version of *TransPore* was used which allowed a full simulation to be computed in less than one second, even when using thousands of experimental times t_i to unroll the boundary conditions (Perré et al., 2015). The inner time step of *TransPore* was adjusted throughout the simulation, not only to secure convergence but also to obtain the simulated results at the exact experimental times (each t_i of Equation 3). The differences between the predicted and experimental values were quantified by the objective function F, defined as the sum of the squared residues:

$$F = \sum_{i=1}^{NT} w_i [m_{exp}(t_i) - m_{pred}(t_i)]^2 \tag{3}$$

where m_{exp} is the experimental sample mass, m_{pred} is the predicted value, ω_i the weighting coefficient, t_i the experimental times, and NT is the number of experimental points.

In this work, we used a uniform weighting factor throughout the test, which means that ω_i is proportional to the time interval between two successive data acquisitions. The optimization algorithm Simplex is used to minimize this function by modifying the unknown parameters (Press et al., 1992). A complete identification requires ca. one minute on a standard personal computer.

For the results discussion, it will be important for the reader to keep in mind that the identified mass diffusivity is corrected from the external resistance and from the coupling between heat and mass. For example, the characteristic times proposed hereafter are therefore "internal characteristic times", solely tied to mass diffusion inside the material.

2.4. Experimental results

Figure 3 exhibits two contrasting examples of raw data (10 and 2 mm of half-thickness), including the actual chamber conditions, together with the best fit as computed with the

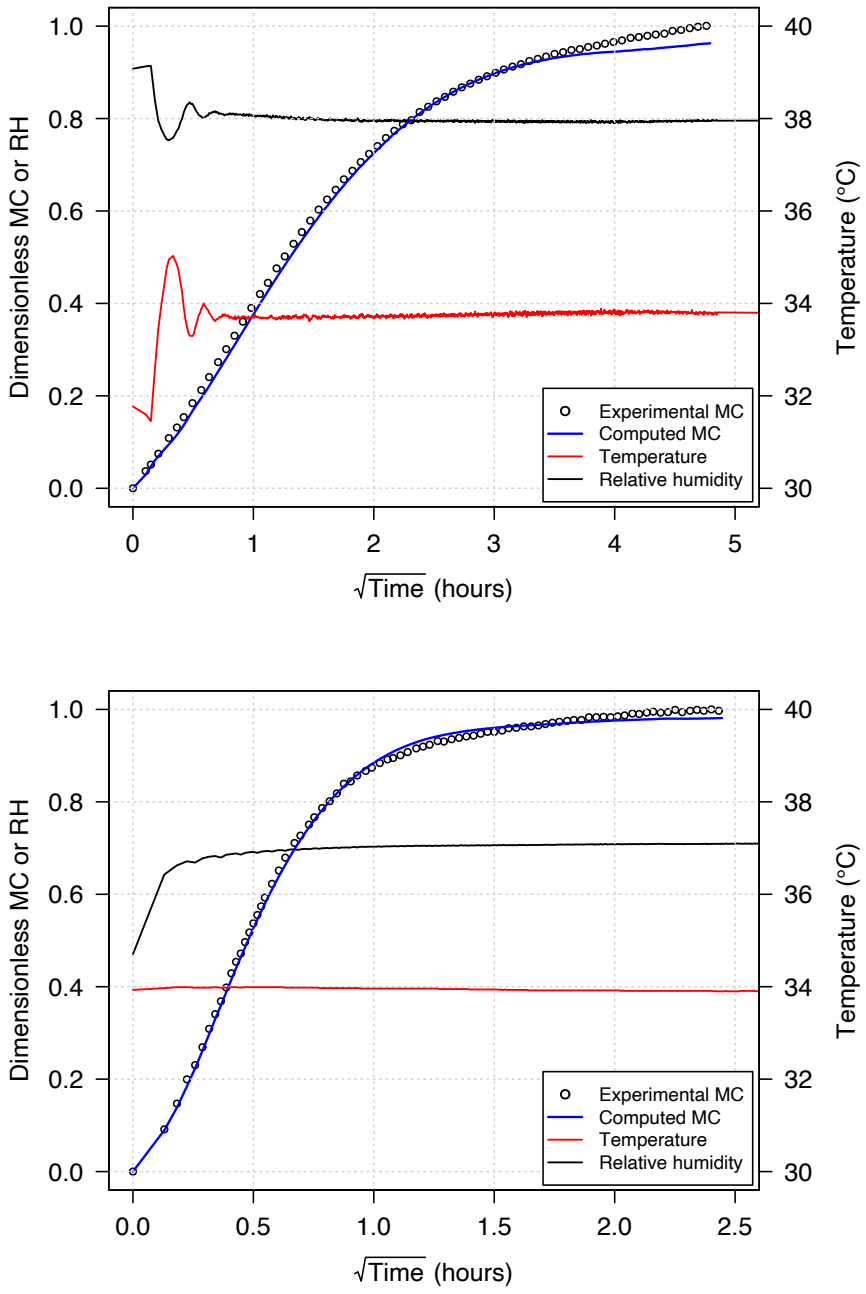

Figure 3: Two examples of simulated sorption behavior after minimization of the objective function for two values of half-thickness: 10 mm (top) and 2 mm (bottom).

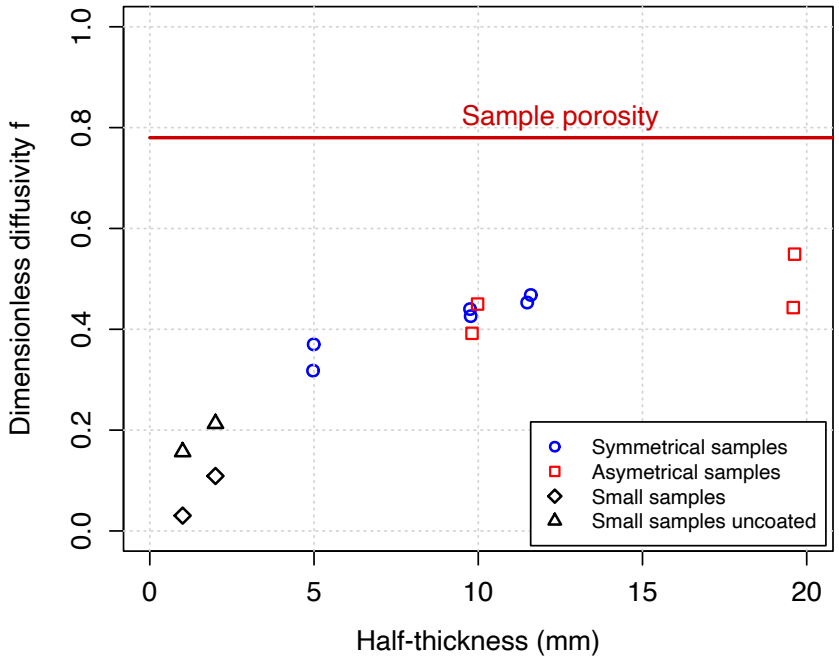

Figure 4: Dimensionless mass diffusivity identified by inverse analysis for all experimental results.

set of identified parameters. Note that the twin climatic chambers used for thick samples (10 mm here) allow the RH step to be very sharp, whereas the RH takes much more time to reach equilibrium in the magnetic suspension balance. This difference is not consequential as the actual chamber conditions are recorded and used as boundary conditions in the inverse procedure. The fit quality is excellent at short times but the slopes are slightly different at longer times, suggesting that the macroscopic model used to fit the data does not encompass all the physics involved in this kind of product. This is confirmed by Figure 4, where the identified values of f are reported as a function of half-thickness. It is obvious that the diffusivity depends strongly on the thickness (Fig. 4), which indicates that this material cannot be represented by an equivalent medium at the macroscopic scale. In such cases, the time constants of phenomena taking place at different spatial levels interfere, which requires the pertinent scales to be considered simultaneously. Additional comments can be drawn from this figure:

- An asymptotic behavior is observed for the higher thickness values, which suggests that the macroscopic time constant eventually dominates,
- Despite the strong heat and mass coupling existing in low-density fiberboard (Perre et al., 2019), the symmetrical and asymmetrical samples draw a unique master curve, which proves that the macroscopic formulation and the proposed boundary conditions are able to rigorously consider this coupling,
- The asymptotic behavior is close to 0.5, which represents a tortuosity factor of ca. 1.56, a consistent value for such a high porosity (Louerat et al., 2018).

Even though we know that the coupling between heat and mass transfer slows the diffusion, an order of magnitude of the time constant τ (in seconds) can be obtained from the diffusivity value and the sample thickness. This value is therefore an "internal characteristic time" accounting for pure mass transfer:

$$\tau = \frac{\ell^2}{D} \tag{4}$$

where ℓ is half the sample thickness for symmetrical conditions(m), and D is the diffusivity ($m^2.s^{-1}$). For this expression to be valid, the accumulation term and the driving force should be consistent. As the diffusivity f is a dimensionless factor acting on the diffusivity of water vapor in air, the slope of the sorption isotherm and the ratio of phase densities should be involved to determine the correct accumulation term. It is evaluated here as the ratio of the respective gaps of moisture constant and relative humidity during the RH step imposed on the sample. Finally, we get the following equation for the time constant:

$$\tau = \frac{\ell^2}{f D_v} \times \frac{RT\rho_s}{P_{vs}(T)M_v} \times \frac{\Delta RH}{\Delta X_{eq}} \tag{5}$$

Using this expression, the internal time constants of mass transfer obtained for all samples are plotted as a function of thickness (Fig. 5). The red line represents the expected trend of this time constant for ideal Fickian behavior. This value is computed from equation (5) using a constant value for f, the one obtained for the thicker samples. This plot confirms that the behavior tends towards a Fickian behavior for large thicknesses. In contrast, instead of a decreasing trend, the time constant depicts asymptotic, constant values for small thicknesses. This asymptotic value is likely to be the microscopic time constant. A comprehensive dual-scale model will be used in the following discussion to confirm and quantify this fact.

3. Comprehensive dual-scale approach

Coupled transfer in heterogeneous media could lead to the failure of local equilibrium (assumptions **A1** and **A2** of the macroscopic formulation). Classical two-scale approaches for flow in porous media assume that at each point in the macroscopic domain, a unit cell exists that is representative of the underlying pore geometry at that point. A set of transport equations is proposed to describe the global (macroscopic) flow, and a separate set of equations is used to describe the local (microscopic) flow. The typical two-scale coupling strategy (Arbogast et al., 1990; Cook and Showalter, 1995; Hornung, 1997; Szymkiewicz and Lewandowska, 2008) is to impose the macroscopic values on the microscopic field via Dirichlet boundary conditions and to include a source term at the macroscopic level that represents the exchange (from the microscale to the macroscale) across the unit cell boundary. This so-called distributed micro-model approach is well adapted to LDF provided that the storage phase does not contribute to the macroscopic fluxes (Fig. 6). A comprehensive formulation suitable for distributed microstructure models in the case of coupled heat and mass transfer, considering the total gaseous pressure through the balance equation of dry air, has been proposed in Perré (2010); Perré (2019). The proposed set of equations involves three independent state variables at both the macroscopic and microscopic scales with relevant coupling equations between scales. For the sake of readability, the detailed description of this formulation is proposed in Appendix B. The task of solving the dual-scale formulation is very challenging for several reasons:

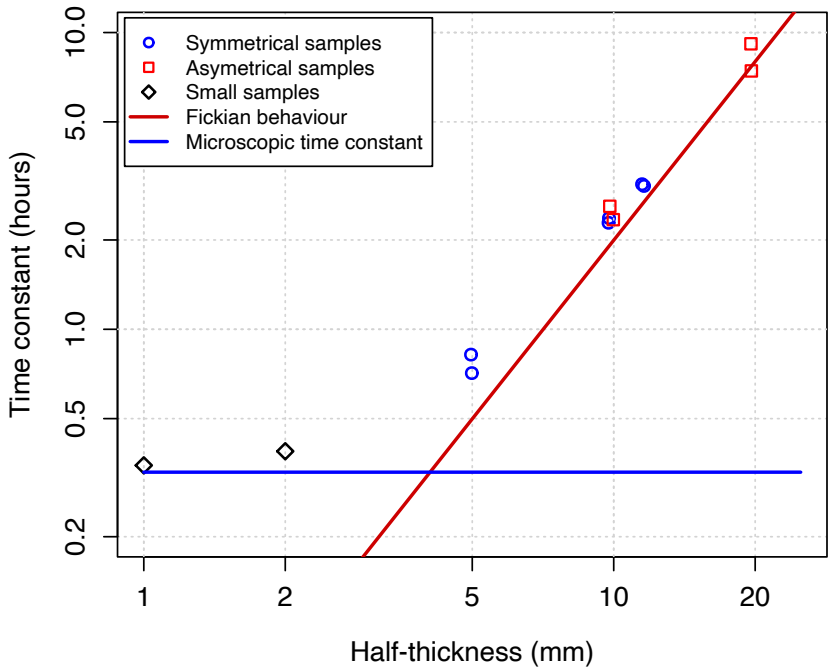

Figure 5: Characteristic diffusion times (internal characteristic time of mass transfer) obtained by Equation 5 as a function of sample thickness. The red line represents the expected trend of this time constant for an ideal Fickian behavior.

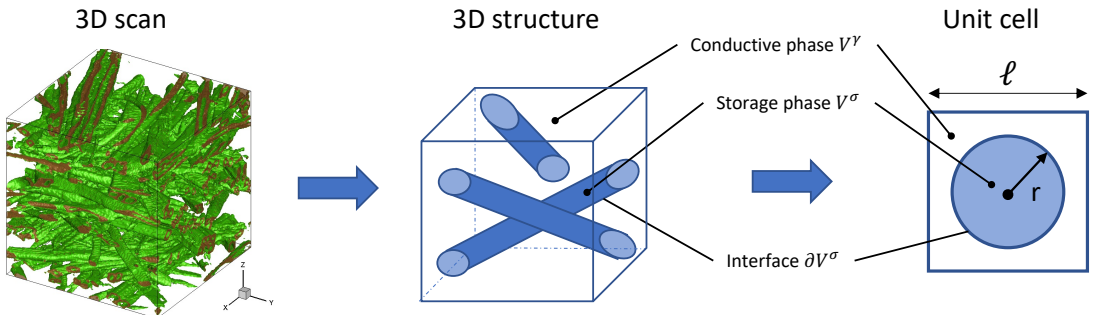

Figure 6: A reasonable unit cell to represent the fiberboard panel at the microscopic level: γ = storage phase, σ = conductive phase.

- A dual-scale approach requires the fields of all micro-models (one per mesh position of the macroscopic domain) to be updated along the macroscopic time,
- The two-way coupling between scales (evolution of boundary conditions imposed to the micro-models and source/sink terms transferred at the macroscopic level) add strong coupling and non-linearities in comparison to the macroscopic model,
- The low moisture inertia of the macroscopic phase results in an extremely stiff coupling between scales.

The coupling between scales was embedded in the Newton–Raphson strategy to reduce CPU time, where the change in the macroscopic variables was used to compute the effect of coupling on the microscopic field, hence the macroscopic source term in the Jacobian. The macroscopic time step evolves along the simulation depending on the global convergence condition, whereas each micro-model continuously adapts its microscopic time step to advance by one macroscopic time step. Owing to this full coupling strategy, the CPU time was reduced to a few minutes (between 3 and 10 minutes depending on the configuration) for 25 control volumes (CVs) at the macroscopic level and 21 CVs for each micro-model. Further detail may be found in Perré (2019). The geometrical factor $A_S/|Y|$ (m^2/m^3) involved in Equation (B.10) is the area of exchange surface between phases γ and σ per unit of macroscopic volume. For the unit cell shape depicted in Figure 6, the calculation of this geometrical factor is straightforward (Table 1). It is expressed a a function of the macroscopic density here, as this macroscopic value is directly tied to the panel density.

Table 1: Geometrical characteristics for the unit cell depicted in Figure 6. L_0 is the unit length in the cylinder direction.

Unit cell volume	$\ell^2 L_o$
Particle volume	$\pi r^2 L_o$
Exchange surface	$2\pi r L_o$
Macroscopic porosity (ϕ_{mac})	$1 - \dfrac{\pi r^2}{\ell^2}$
Geometrical factor ($A_\sigma/\|V\|$)	$\dfrac{2(1-\phi_{mac})}{r}$

Several physical parameters must be supplied to the dual-scale model (Table 2). Thermal conductivity, dimensionless diffusivity and gaseous permeability are among the key macroscopic parameters for the experimental configuration of interest here. The thermal conductivity was quite accurately determined by the internal temperature rise at the center of panels during transient sorption tests Perre et al. (2019). In addition, this value is in good agreement with values available in the literature for panels of the same density Rebolledo et al. (2018); Lee et al. (2019). The dimensionless diffusivity f should be the actual value of water vapor diffusion in the connected gaseous phase at very large thicknesses. The value 0.53 is consistent with both the asymptotic trend observed at large

thicknesses (Fig. 4) and with the value computed on real 3D morphologies Louerat et al. (2018). At the microscopic scale, the thermal conductivity is sufficient to ensure a uniform temperature inside the microscopic inclusion, which might, however, be different from the gaseous temperature due to coupling transfers at the interface. Therefore, the fiber diameter and the mass diffusivity are the key microscopic parameters. Together, they determine the microscopic time constant and are, therefore, not independent parameters. We choose to fix the fiber diameter, which is quite easy to determine by microscopic observation, and keep the mass diffusivity as a degree of freedom. Morphological observations with an environmental scanning electron microscope (ESEM, FEI Quanta 200) show that the solid phase is primarily composed of isolated fibers with a diameter in the range of 30 μm to 50 μm, together with a few fiber aggregations (Almeida et al., 2018). The inclusion radius was then set at $20\,\mu m$. The solid density (1200 $kg.m^{-3}$) is less than the cell wall density (1500 $kg.m^{-3}$) to correct for the inner porosity of fibers and therefore obtain a better evaluation of the macroscopic porosity. As the unit cell is simply a cylinder centered in a rectangular box of square section, the macroscopic porosity is computed from the macroscopic density. Geometrical considerations allow then to compute the geometrical factor, which represents the surface area of solid/pore interface per macroscopic volume.

Two different values of heat transfer coefficients were used to analyze the experimental data, to account for each specific device. In this simulation part, for the sake of simplicity, a unique value was used. This is not important as the same value was used to generate the dual-scale data and, subsequently, in the macroscopic model to identify the equivalent macroscopic value.

Table 2: Values of the key parameters used in the dual-scale simulations.

Radius of the microscopic particle	$20\,\mu m$
Density of the microscopic particle	$1200\,kg.m^{-3}$
Macroscopic porosity	0.7875
Geometrial factor ($A_\sigma / \lvert V \rvert$)	21250
Macroscopic diffusivity $\boldsymbol{D}^\sigma_{eff}$	$0.53 \times \boldsymbol{D}_v$
Macroscopic thermal conductivity λ^σ_{eff}	$0.05\,W.K^{-1}.m^{-1}$
Macroscopic heat transfer coefficient h^σ_h	$25\,W.K^{-1}.m^{-2}$
Macroscopic mass transfer coefficient h^σ_m	$0.025\,m.s^{-1}$

4. Dual-scale results and discussion

This dual-scale model has been used to generate a database with a wide range of half-thicknesses (1, 2, 3, 4, 5, 7, 10, 15 and 20 mm) and a set of microscopic diffusivity values (1.10^{-14}, 3.10^{-14}, 1.10^{-13}, 3.10^{-13} and 1.10^{-12} $m^2.s^{-1}$) that represent a total of 45 simulations. Figure 7 depicts the results obtained for two contrasting examples of such dual-scale

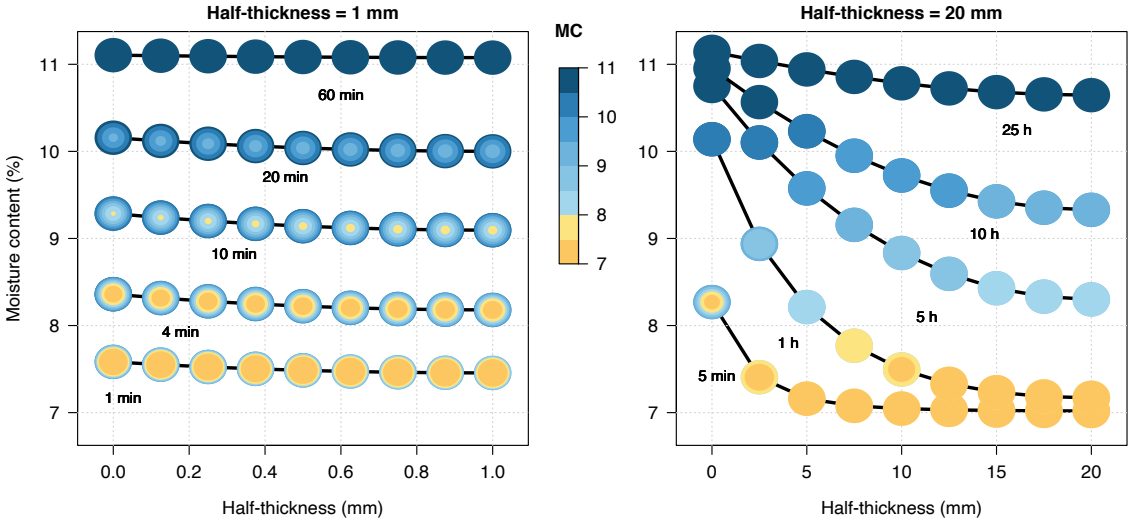

Figure 7: Two contrasted results of the dual-scale model (microscopic mass diffusivity equal to $10^{-13} m^2.s^{-1}$); left) sample thickness of 1 mm and right) sample thickness of 20 mm. The solid lines represent the macroscopic profiles at selected times, and the colored circles represent the profiles inside a subset of microscopic cells. The exchange surface is at $x = 0$, and the highest x value is at the plane of symmetry.

simulations. Two different thicknesses (1 mm and 20 mm of half-thickness) were selected for the same value of microscopic diffusivity ($1.10^{-13}\, m^2.s^{-1}$). For each plot, macroscopic profiles are plotted at selected times (MC on the y-axis versus position on the x-axis, with the exchange face at $x = 0$). In addition, the moisture content (MC) field inside the microscopic fiber is plotted as colored isovalues in a sub-set of micromodels evenly distributed over the thickness. The scale of this microscopic field (colored legend) is the same as the macroscopic fields, as initial and equilibrium MC values are the same at both scales. The intentionally chosen thicknesses depict extreme behaviors:

- For the 1-mm test, the macroscopic profiles remain almost flat. However, the isovalues confirm that the microscopic fields are not at equilibrium at all. In this extreme case of a thin sample, the behavior is almost entirely controlled by the microscopic diffusion inside the storage phase. The macroscopic resistance to vapor diffusion in the connected pores remains negligible, and all fibers undergo similar conditions,
- The opposite behavior is observed for the 20-mm thick sample. With such a thickness, the resistance to macroscopic diffusion through the conductive phase becomes the dominant effect. Except at the exchange surface and short times, the internal profiles inside fibers are almost uniform, and classical diffusion profiles develop over time and along position at the macroscopic scale.

The gradients at the microscopic and macroscopic scales were plotted as MC differences to better quantify these trends. In Figure 8, these differences were plotted for the same configuration as for figure 7:

- the black line is the difference of macroscopic MC ($X_{surface} - X_{core}$),
- the red line is the MC gap for the fiber at the exchange surface of the sample,

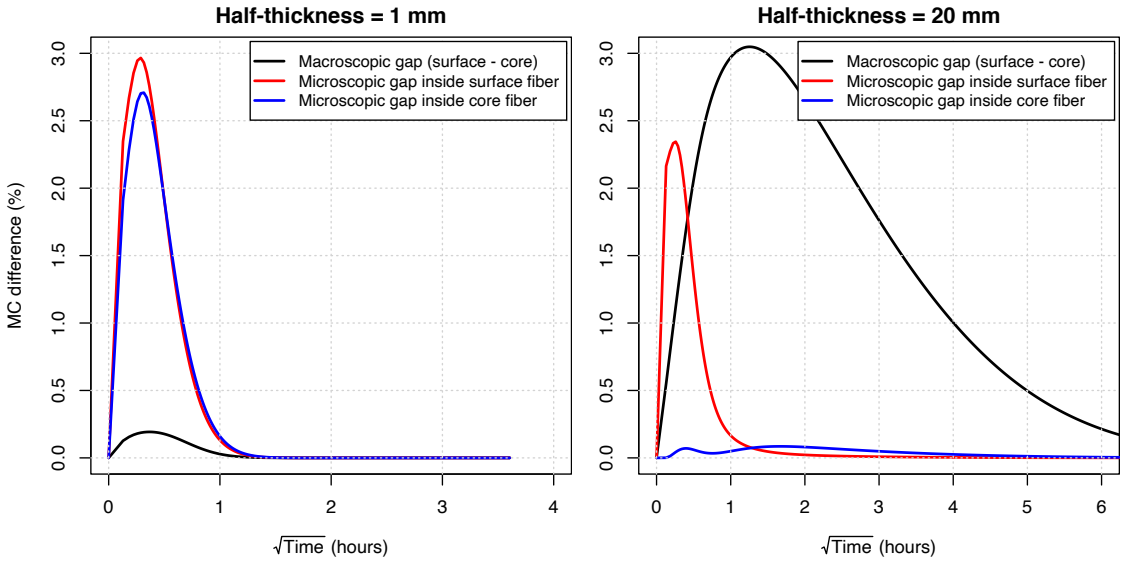

Figure 8: Evolution of the moisture content gradient (gap between surface and core) at the macroscopic and microscopic levels, using the same tests as Figure 7. For the gap inside the microscopic cell, the two extreme behavior are plotted (surface fiber and core fiber. left) sample thickness of 1 mm and right) sample thickness of 20 mm.

- the blue line is the MC gap for the fiber at the plane of symmetry.

For the thin sample (1 mm), figure 8 confirms that the MC gradients in the surface and core fiber are very similar. The effect of diffusion along the sample thickness affects the behavior (blue line slightly lower than the red line) to a small extent. The gap increases rapidly at short times, reaches a maximum and then decreases until equilibrium. For this value of $1.10^{-13}\, m^2.s^{-1}$ for the microscopic diffusivity and a radius of $20\,\mu m$, the microscopic time constant is of the order of one hour. The macroscopic MC gap (black line) remains negligible. In the case of the thick sample (20 mm), we still can observe an MC gap in the fiber at the surface (red line). This is consistent, as this fiber placed at the exchange surface undergoes similar conditions as the thin sample. However, the characteristic time is now shorter than the macroscopic characteristic time. The MC gap throughout the sample thickness now develops over several hours and controls the physical behavior. The evolution of conditions at the core of the sample is now sufficiently slow for the core fiber to increases in MC with a quasi-uniform MC field, as depicted by the blue line. The slight bump observed on this blue line at a very short time (ca. 0.2 hour) results from the coupling between heat and mass transfer: the sudden condensation at the surface releases the latent heat of vaporization and heats the surface. This generates a driving force for water vapor diffusion by the increase of saturated vapor pressure, which turns into condensation in the sample core. The interested reader might refer to (Perre et al., 2019) for a detailed analysis of this coupling.

The respective effects of microscopic and macroscopic effects depend on the two parameters varying in our simulation database (thickness and microscopic diffusivity). The dual-scale results were analyzed by the same inverse method to compare these simulations with the experimental data. This means that the computed time evolution of the average MC

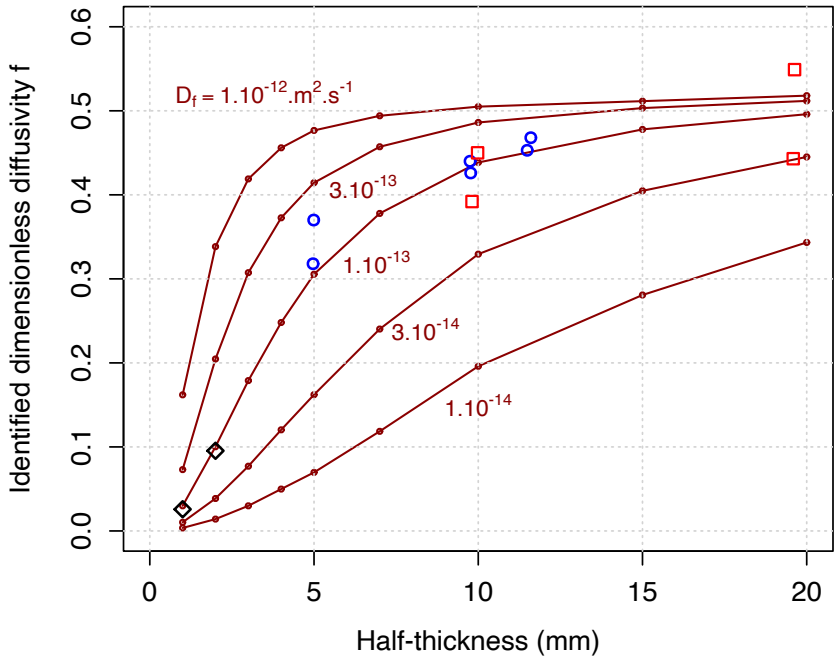

Figure 9: Dual scale simulations: apparent macroscopic diffusivity identified with the macroscopic model as a function of sample thickness for different values of the microscopic (fiber) diffusivity. The markers are the experimental values identified in Section 2.4.

predicted by the dual scale model was used as input data in the inverse procedure using the macroscopic formulation (§ 2.3 - Fig. 1) to identify the value of f. The whole set of results is plotted in (Fig. 9) and summarized in Table 3. The microscopic diffusivity shifts the transition from a microscopic-dominant behavior to a macroscopic-dominant one. For example, this transition of the half-thickness ranges from $0.5-5\,mm$, to $1-20\,mm$ and $3-50\,mm$ for respective values of microscopic diffusivity of 1.10^{-14}, 1.10^{-13} and 1.10^{-12} $m^2.s^{-1}$. The experimental values were also plotted as markers in Figure 9, which indicates that a microscopic diffusivity of $1.10^{-13}\,m^2.s^{-1}$ gives trends in very good agreement with the experimental values. This is also evidenced by the values in Table 3.

To extrapolate the outcomes of this works to fiberboard panels of different densities, we assume the microscopic behavior to similar and used the expression proposed in (Louerat et al., 2018) to obtain the macroscopic diffusivity f as a function of the solid fraction:

$$f = (\epsilon_s f_s^\alpha + \epsilon_g f_g^\alpha)^{1/\alpha} \tag{6}$$

with $f_s = 0.004$ and $f_g = 1$. The value of α, 0.18, was obtained in (Louerat et al., 2018) by the best fit from the values computed on real 3D morphologies. In this work, the porosity was obtained by segmentation of high-resolution 3D scans and included the internal porosity: therefore, the solid fraction must be computed by the actual density of cell walls ($1500\ kg.m^{-3}$). It is worth mentioning that the f value predicted by expression

Table 3: Dimensionless vapor diffusivity obtained for different simulations, as compared to the experimental data.

Fibre diffusivity	Half-thickness (mm)								
D_f ($m^2.s^{-1}$)	1	2	3	4	5	7	10	15	20
1.10^{-14}	0.0036	0.0141	0.0290	0.0498	0.0697	0.118	0.196	0.281	0.343
3.10^{-14}	0.0103	0.0386	0.0771	0.120	0.162	0.240	0.329	0.404	0.445
1.10^{-13}	0.0299	0.100	0.179	0.248	0.305	0.378	0.438	0.478	0.496
3.10^{-13}	0.073	0.204	0.307	0.373	0.414	0.457	0.486	0.503	0.511
1.10^{-12}	0.162	0.338	0.419	0.456	0.477	0.494	0.505	0.508	0.518
Experiment	0.0304	0.109			0.318 0.370		0.426 0.440		0.443 0.549

(6) for a panel of $255\,kg.m^{-3}$ gives a value of 0.533 very close to the value obtained as asymptotic behavior for large thickness values (Fig. 4). We must, however, keep in mind that such a good agreement results from a consistent consideration of heat and mass transfer coupling. In Louerat et al. (2018), the computational method allows pure mass transfer at the pore level to be considered, without any coupling with heat transfer. The physical engine properly considers the heat and mass coupling in the inverse procedure used to identify the macroscopic diffusivity. Without such a comprehensive model, the mass diffusivity would have been underestimated by a factor almost equal to 0.5 (see Table 1 of (Perre et al., 2019)).

Combining Equations (5) and (6) allowed us to compute the characteristic time constant of macroscopic diffusion as a function of panel density and thickness (Fig. 10). Remember that the characteristic time constant of the microscopic phase is of the order of one hour. The dual-scale effects must be kept for a macroscopic time constant of less than 2 hours and, according to Figure 5, can be neglected above 4 hours. The main conclusions of this work are:

- A non-Fickian behavior of transient diffusion was confirmed by our experimental data, and we prove that this non-Fickian behavior is mainly due to the dual-scale effect,
- The comparison of experimental and dual-scale data permits a microscopic behavior (combination of diffusivity and size) able to predict that for a radius of $20\,\mu m$, the relevant microscopic diffusivity is close to $1.10^{-13}\,m^2.s^{-1}$,
- With these values, a panel of $255\,kg.m^{-3}$ whose total thickness is larger than ca. $4\,cm$ is controlled by the macroscopic behavior.

Important practical recommendations might be drawn from these conclusions. At first sight, this dual-scale effect can be neglected for thick panels in building energy simulation (BES) models. A chart is proposed to evaluate the required thickness as a function of the fiberboard panel density. However, it is important to point out two major exceptions:

1. Dual-scale effects should be accounted for material characterization for the determined values to be valid at the building level, where thicknesses are likely to be larger,

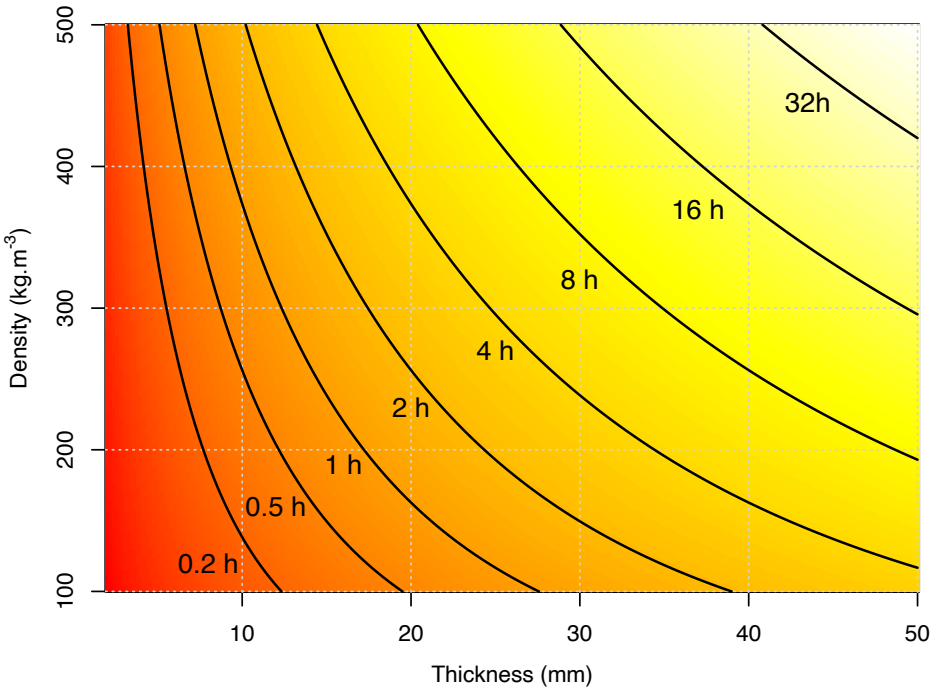

Figure 10: Characteristic time constant of macroscopic diffusion as a function of panel density and thickness (the full thickness is plotted here). Remember that the characteristic time constant of the microscopic phase is of the order of one hour. The dual-scale effects must be kept for a macroscopic time constant of less than 2 hours and can be neglected above 4 hours.

2. Dual-scale effects must be considered at the building level to properly account for the moisture buffering effect that might affect only thin layers of the envelope. In these cases of transient transfer, the dual-scale effect also explains the delay between relative humidity and moisture content, which remains challenging in BES models (Lelievre et al., 2014; Challansonnex et al., 2019).

The formulation detailed in Perré (2019) proposes a quite simple way to include this dual-scale effect in the macroscopic formulation. According to the range of thickness over which dual-scale effects matter, we recommend including one single exponential term in this formulation.

5. Conclusion

This work is devoted to the diffusion mechanisms in low-density fiberboards (LDF). Experiments performed in a transient regime exhibit an effect of the sample thickness that does not obey Fickian's law. We used a comprehensive dual-scale model, accounting for the coupling between heat and mass transfer both at microscopic and macroscopic scales to address this situation. The comparison between experimental and simulated results proved that the dual-scale effect nicely explains the observed mechanisms. A good fit with the experimental data is obtained for a microscopic diffusivity of the storage phase equal to $1.10^{-13}\, m^2.s^{-1}$ for a fiber radius of $20\, \mu m$. We recommend that the dual scale effect be neglected for this kind of fiberboard for a total thickness larger than ca. 4 cm: this also means that this effect must be considered in characterization or to capture the buffering effect of the external surfaces of the envelope.
Ongoing work aims to test these dual-scale effects, as well as a sorption hysteresis model (Rémond et al., 2018), on experimental data obtained at the wall scale with periodic conditions, for which a classical macroscopic model fails.

Acknowledgement

This study was carried out in the Centre Européen de Biotechnologie et de Bioéconomie (CEBB), supported by the Région Grand Est, Département de la Marne, Greater Reims and the European Union. In particular, the authors would like to thank the Département de la Marne, Greater Reims, Région Grand Est and the European Union along with the European Regional Development Fund (ERDF Champagne Ardenne 2014-2020) for their financial support of the Chair of Biotechnology of CentraleSupélec. This study was also conducted with a partial support of the project Smart-Réno.

CRediT author statement

PP: Conceptualization, Methodology, Formal analysis, Modeling, Simulation, Visualization, Writing-Original draft preparation, Writing-Reviewing and Editing, Supervision, Funding acquisition. RR: Investigation, Methodology, Formal analysis, Writing-Reviewing and Editing GA: Conceptualization, Investigation, Methodology, Formal analysis, Writing-Reviewing and Editing.

References

Agoua, E., Zohoun, S., Perré, P., 2001. A double climatic chamber used to measure the diffusion coefficient of water in wood in unsteady-state conditions: determination of the best fitting method by numerical simulation (in French). International Journal of Heat and Mass Transfer 44, 3731–3744.

Almeida, G., Rémond, R., Perré, P., 2018. Hygroscopic behaviour of lignocellulosic materials: Dataset at oscillating relative humidity variations. Journal of Building Engineering 170, 716–724.

Arbogast, T., J. Douglas, J., Hornung, U., 1990. Derivation of the double porosity model of single phase flow via homogenization theory. SIAM Journal on Mathematical Analysis 21, 823–836.

Busser, T., Berger, J., Piot, A., Pailha, P., Woloszyn, M., 2018. Dynamic experimental method for identification of hygric parameters of a hygroscopic material. Building and Environment 131, 197—209.

Challansonnex, A., Casalinho, J., Perré, P., 2019. Non-fickian diffusion in biosourced materials: Prediction of the delay between relative humidity and moisture content. Energy and Buildings 202, 109340.

Christensen, G., 1967. Sorption and Swelling within Wood Cell Walls. Nature 213, 782–784.

Colin, J., Rémond, R., Perre, P., 2016. Design and optimization of industrial woody biomass pretreatment addressed by drykiln_crp, a multiscale computational model: Particle, bed, and dryer levels. Drying Technology 34, 1820–1830.

Cook, J.D., Showalter, R.E., 1995. Microstructure diffusion models with secondary flux. Journal of Mathematical Analysis and Applications 189, 731–756.

Crawley, D., Lawrie, L., Winkelmann, F., Buhl, W., Huang, Y., Pedersen, C., Strand, R., Liesen, R., Fisher, D., Witte, M., et al., 2001. Energyplus: creating a new-generation building energy simulation program. Energy and buildings 33, 319–331.

Delgado, J., Ramos, N., Barreira, E., De Freitas, V., 2010. A critical review of hygrothermal models used in porous building materials. Journal of Porous Media 13.

Downes, J., Mackay, B., 1958. Sorption kinetics of water vapor in wool fibers. Journal of Polymer Science 28, 45–67.

Frandsen, L., Svensson, S., Damkilde, L., 2007. A hysteresis model suitable for numerical simulation of moisture content in wood. Holzforschung 61, 175–181.

Ge, H., Yang, X., Fazio, P., Rao, J., 2014. Influence of moisture load profiles on moisture buffering potential and moisture residuals of three groups of hygroscopic materials. Building and Environment 81, 162–171.

Hornung, U. (Ed.), 1997. Homogenization and porous media. Springer–Verlag, New York.

Jacques, J., Labat, M., Woloszyn, M., 2015. Dynamic coupling between vapour and heat transfer in wall assemblies : Analysis of measurements achieved under real climate. Building and Environment 87, 129–141.

Krabbenhoft, K., Damkilde, L., 2004. Double porosity models for the description of water infiltration in wood. Wood Science and Technology 38, 641–659.

Künzel, H., Holm, A., Zirkelbach, D., Karagiozis, A., 2005. Simulation of indoor temperature and humidity conditions including hygrothermal interactions with the building envelope. Solar Energy 78, 554–561.

Kwiatkowski, J., Woloszyn, M., Roux, J., 2011. Influence of sorption isotherm hysteresis effect on indoor climate and energy demand for heating. Applied Thermal Engineering 31, 1050–1057.

Lee, M., Lee, S.M., Kang, E.C., 2019. Changes in characteristics of wood fiber insulation board according to density. BioResources 14, 6529–6543.

Lelievre, D., Colinart, T., Glouannec, P., 2014. Hygrothermal behavior of bio-based building materials including hysteresis effects: Experimental and numerical analyses. Energy and Buildings 84, 617–627.

Louerat, M., Ayouz, M., Perré, P., 2018. Heat and moisture diffusion in spruce and wood panels computed from 3-D morphologies using the Lattice Boltzmann method. International Journal of Thermal Sciences 130, 471–483. doi:10.1016/j.ijthermalsci.2018.05.009.

Merakeb, S., Dubois, F., Petit, C., 2009. Modélisation des hystérésis de sorption dans les matériaux hygroscopiques. Comptes Rendus Mécanique 337, 34–39.

Nyman, U., Gustafsson, P., Johannesson, B., Hägglund, R., 2006. A numerical method for the evaluation of non-linear transient moisture flow in cellulosic materials. International Journal for Numerical Methods in Engineering 66, 1859–1883.

Perré, P., 2010. Multiscale modelling of drying as a powerful extension of the macroscopic approach: application to soid wood and biomass processing. Dry. Technol. 28, 944–959.

Perré, P., 2015. The proper use of mass diffusion equations in drying modeling: Introducing the drying intensity number. Drying Technology 33, 1949–1962.

Perré, P., 2019. Coupled heat and mass transfer in biosourced porous media without local equilibrium: a macroscopic formulation tailored to computational simulation. Int. J. Heat Mass Transfer 140, 717–730.

Perre, P., Challansonnex, A., Colin, J., 2019. On the importance of heat and mass transfer coupling for the characterization of hygroscopic insulation materials. International Journal of Heat and Mass Transfer 133, 968–975.

Perré, P., Houngan, A., Jacquin, P., 2007a. Mass diffusivity of beech determined in unsteady-state using a magnetic suspension balance. Drying Technology 25, 1341–1347.

Perré, P., May, B., 2007. The existence of a first drying stage for potato proved by two independent methods. Journal of food engineering 78, 1134–1140.

Perré, P., Pierre, F., Casalinho, J., Ayouz, M., 2015. Determination of the mass diffusion coefficient based on the relative humidity measured at the back face of the sample during unsteady regimes. Drying Technology 33, 1068–1075.

Perré, P., Remond, R., Turner, I.W., 2007b. Comprehensive drying models based on volume averaging: Background, application and perspective, in: Tsotsas, E., Mujumdar, A.S. (Eds.), Drying Technology: Computational Tools at Different Scales. Wiley-VCH. volume 1.

Perré, P., Turner, I.W., 1999. A 3D version of Transpore: a comprehensive heat and mass transfer computational model for simulating the drying of porous media. International Journal for Heat and Mass Transfer 42, 4501–4521.

Press, W., Teukolsky, S., Vetterling, W., Flannery, B., 1992. Numerical recipes in FORTRAN: The art of scientific computing. Cambridge University Press, New York.

Rebolledo, P., Cloutier, A., Yemele, M.C., 2018. Effect of density and fiber size on porosity and thermal conductivity of fiberboard mats. Fibers 6, 81.

Rémond, R., Almeida, G., 2011. Mass diffusivity of low-density fibreboard determined under steady-and unsteady-state conditions: Evidence of dual-scale mechanisms in the diffusion. Wood Material Science and Engineering 6, 23–33.

Rémond, R., Almeida, G., Perré, P., 2018. The gripped-box model: A simple and robust formulation of sorption hysteresis for lignocellulosic materials. Construction and Building Materials 170, 716–724.

Silva, O., Carrera, J., Dentz, M., Kumar, S., Alcolea, A., Wilmann, M., 2009. A general real-time formulation for multi-rate mass transfer problems. Hydrology and Earth System Sciences 13, 1399–1411.

Szymkiewicz, A., Lewandowska, J., 2008. Micromechanical approach to unsaturated water flow in structured geomaterials by two-scale computations. Acta Geotechnica 3, 37–47.

Welty, J.R., Wicks, C.E., Rorrer, G., Wilson, R.E., 2009. Fundamentals of momentum, heat, and mass transfer. John Wiley & Sons.

Woloszyn, M., Rode, C., 2008. Tools for performance simulation of heat, air and moisture conditions of whole buildings, in: Building Simulation, Springer. pp. 5–24.

Appendix A. Macroscopic formulation of coupled heat and mass transfer

The comprehensive macroscopic formulation of coupled heat and mass transfer in porous media is well-established and was already used in building materials (Perré and Turner, 1999; Perre et al., 2019). It is detailed in this appendix to avoid the reader to refer to the published papers. This

formulation assumes, water to exist in three different forms: liquid, vapor and bound water. For the sake of simplification, all liquid water contributions have been discarded in the present work, as the sample stays inside the hygroscopic domain. Similarly, considering the particular morphology of fiberboard, one can assume that a very large majority of the mass transfer occurs in the gaseous phase. Thus, the transport terms of bound water have been discarded.

Moisture conservation

$$\rho_s \frac{\partial X}{\partial t} + \nabla \cdot (\rho_v \overline{\boldsymbol{v}}_g) = \nabla \cdot (\rho_g \boldsymbol{f} \boldsymbol{D}_v \cdot \nabla \omega_v) \tag{A.1}$$

Energy conservation

$$\frac{\partial}{\partial t}\left(\varepsilon_g(\rho_v h_v + \rho_a h_a) + \overline{\rho}_b \overline{h}_b + \varepsilon_s \rho_s h_s\right) + \nabla \cdot ((\rho_v h_v + \rho_a h_a)\overline{\boldsymbol{v}}_g) = \nabla \cdot (\lambda_{eff} \nabla T + \rho_g \boldsymbol{f} \boldsymbol{D}_v (h_v \nabla \omega_v + h_a \nabla \omega_a)) \tag{A.2}$$

Air conservation

$$\frac{\partial\left(\varepsilon_g \rho_a\right)}{\partial t} + \nabla \cdot (\rho_a \overline{\boldsymbol{v}}_g) = \nabla \cdot (\rho_g \boldsymbol{f} \boldsymbol{D}_v \nabla \omega_a) \tag{A.3}$$

Boundary conditions, exposed face

$$\begin{aligned} &\boldsymbol{q}_v|_{x=0^+} \cdot \boldsymbol{n} = h_m \, c \, M_v \, \ln\left(\frac{1 - x_\infty}{1 - x_v|_{x=0}}\right) \\ &\boldsymbol{q}_h|_{x=0^+} \cdot \boldsymbol{n} = h_h \left(T|_{x=0} - T_\infty\right) \\ &P_g|_{x=0^+} = P_{atm} \end{aligned} \tag{A.4}$$

Boundary conditions, plane of symmetry

$$\begin{aligned} &\boldsymbol{q}_v|_{x=0^+} \cdot \boldsymbol{n} = 0 \\ &\boldsymbol{q}_h|_{x=0^+} \cdot \boldsymbol{n} = 0 \\ &\rho_a \overline{\boldsymbol{v}}_a|_{x=0^+} = 0 \end{aligned} \tag{A.5}$$

Boundary conditions, mass-insulated face

$$\begin{aligned} &\boldsymbol{q}_v|_{x=0^+} \cdot \boldsymbol{n} = 0 \\ &\boldsymbol{q}_h|_{x=0^+} \cdot \boldsymbol{n} = h_h \left(T|_{x=0} - T_\infty\right) \\ &\rho_a \overline{\boldsymbol{v}}_a|_{x=0^+} = 0 \end{aligned} \tag{A.6}$$

In these equations, the barycentric gas velocity comes from the generalized Darcy's law, in which gravity has been neglected and where the relative permeability to the gaseous phase was set to the unit:

$$\overline{\boldsymbol{v}}_g = -\frac{\boldsymbol{K}}{\mu_g} \nabla p_g$$

The previous set of equations assumes that the porous medium is locally at equilibrium. This implies that:

A1 the temperature is the same for all phases $T_s = T_g$

A2 the partial pressure of water vapor inside the gaseous phase is related to the moisture content X *via* the sorption isotherm $p_v = p_{vs}(T) \times a(T, X)$, where function a is the sorption isotherm of the product, which gives the water activity of the fibers as function of X and T.

Appendix B. Formulation of the dual-scale approach

This so-called distributed micro-model approach is well adapted provided that the storage phase does not contribute to the macroscopic fluxes. A formulation is suitable for distributed microstructure models in the case of coupled heat and mass transfer, considering the total gaseous pressure

through the balance equation of dry air proposed in Perré (2019). This formulation involves three independent state variables at both the macroscopic and microscopic scales. In the following equations, superscript γ denotes the macroscopic scale, and superscript σ denotes the microscopic scale. To avoid confusion with the intrinsic phase of the considered scale, the scale superscript is shifted to the right when a superficial average is involved (for example, $\overline{\boldsymbol{v}}_g{}^{\sigma}$ instead of $\overline{\boldsymbol{v}}_g^{\sigma}$). Ω designs the macroscopic domain, V_σ is the part of the REV V occupied by the storage phase, and ∂V_σ is the interface between the conductive and storage phase inside V. Two space coordinates systems are involved: $\mathbf{x}$ denotes the macroscopic position in Ω, and $\mathbf{y}$ is the position inside the REV V at point $\mathbf{x}$.

Microscopic scale

Moisture conservation

$$\begin{aligned}&\rho_0 \frac{\partial X^\sigma}{\partial t} + \nabla_y \cdot (\rho_w^\sigma \overline{\boldsymbol{v}}_w{}^{\sigma} + \rho_v^\sigma \overline{\boldsymbol{v}}_g{}^{\sigma}) \\ &= \nabla_y \cdot \left(\rho_g^\sigma \boldsymbol{D}_{eff}^\sigma \nabla_y \omega_v^\sigma + \rho_0^\sigma \boldsymbol{D}_b^\sigma \nabla X_b^\sigma\right) \quad y \in V_\sigma(x),\ x \in \Omega\end{aligned} \tag{B.1}$$

Energy conservation

$$\begin{aligned}&\frac{\partial}{\partial t}\left(\varepsilon_w^\sigma \rho_w^\sigma h_w^\sigma + \varepsilon_g^\sigma(\rho_v^\sigma h_v^\sigma + \rho_a^\sigma h_a^\sigma) + \overline{\rho_b h_b}{}^{\sigma} + \varepsilon_s^\sigma \rho_s^\sigma h_s^\sigma - \varepsilon_g^\sigma P_g^\sigma\right) \\ &\qquad + \nabla_y \cdot (\rho_w^\sigma h_w^\sigma \overline{\boldsymbol{v}}_w{}^{\sigma} + (\rho_v^\sigma h_v^\sigma + \rho_a^\sigma h_a^\sigma)\overline{\boldsymbol{v}}_g{}^{\sigma}) \\ &= \nabla_y \cdot \left(\boldsymbol{\lambda}_{eff}^\sigma \nabla_y T^\sigma + (h_v^\sigma - h_a^\sigma)\rho_g^\sigma \boldsymbol{D}_{eff}^\sigma \nabla_y \omega_v^\sigma + h_b^\sigma \rho_0^\sigma \boldsymbol{D}_b^\sigma \nabla X_b^\sigma\right) \quad y \in V_\sigma(x),\ x \in \Omega\end{aligned} \tag{B.2}$$

Air conservation

$$\frac{\partial}{\partial t}\left(\varepsilon_g^\sigma \rho_a^\sigma\right) + \nabla_y \cdot (\rho_a^\sigma \overline{\boldsymbol{v}}_g{}^{\sigma}) = \nabla_y \cdot \left(\rho_g^\sigma \boldsymbol{D}_{eff}^\sigma \nabla_y \omega_a^\sigma\right) \quad y \in V_\sigma(x),\ x \in \Omega \tag{B.3}$$

Macroscopic scale

In the following equations, moisture is assumed to be present only as water vapor in the conductive phase.

Moisture conservation

$$\frac{\partial}{\partial t}\left(\varepsilon_g^\gamma \rho_v^\gamma\right) + \nabla_x \cdot (\rho_v^\gamma \overline{\boldsymbol{v}}_g{}^{\gamma}) = \nabla_x \cdot \left(\rho_g^\gamma \boldsymbol{D}_{eff}^\gamma \nabla_x \omega_v^\gamma\right) + Q_v(t,x) \quad x \in \Omega \tag{B.4}$$

Energy conservation

$$\begin{aligned}&\frac{\partial}{\partial t}\left(\varepsilon_g^\gamma(\rho_v^\gamma h_v^\gamma + \rho_a^\gamma h_a^\gamma)\right) + \nabla_x \cdot ((\rho_v^\gamma h_v^\gamma + \rho_a^\gamma h_a^\gamma)\overline{\boldsymbol{v}}_g{}^{\gamma}) \\ &\qquad = \nabla_x \cdot \left(\rho_g^\gamma \boldsymbol{D}_{eff}^\gamma (h_v^\gamma \nabla_x \omega_v^\gamma + h_a^\gamma \nabla_x \omega_a^\gamma) + \lambda_{eff}^\gamma \nabla_x T^\gamma\right) \\ &\qquad\qquad + Q_h(t,x) + h_v^\gamma Q_v(t,x) + h_a^\gamma Q_a(t,x) \quad x \in \Omega\end{aligned} \tag{B.5}$$

Air conservation

$$\frac{\partial}{\partial t}\left(\varepsilon_g^\gamma \rho_a^\gamma\right) + \nabla_x \cdot (\rho_a^\gamma \overline{\boldsymbol{v}}_g{}^{\gamma}) = \nabla_x \cdot \left(\rho_g^\gamma \boldsymbol{D}_{eff}^\gamma \nabla_x \omega_a^\gamma\right) + Q_a(t,x) \quad x \in \Omega \tag{B.6}$$

Coupling between scales

A two-way coupling holds between the microscopic and macroscopic scales: the boundary conditions applied at the local scale involve the macroscopic variables, and the integration of the fluxes on the contour of the micro-model builds up the source terms to be supplied at the macroscopic

level. These couplings are summarized hereinafter:

Moisture exchange

$$\begin{aligned}
&\rho_g^\sigma \boldsymbol{D}_{eff}^\sigma \nabla_y \omega_v^\sigma \cdot \boldsymbol{n} = h_m^\sigma \rho_g^\sigma \ (\omega_v^\sigma(t,x,y) - \omega_v^\gamma(t,x)) \quad y \in \partial V^\sigma(x), \quad x \in \Omega \\
&Q_v(t,x) = \frac{1}{|V|} \int_{\partial V^\sigma(x)} \rho_g^\sigma \boldsymbol{D}_{eff}^\sigma \nabla_y \omega_v^\sigma \cdot \boldsymbol{n} \, dS \quad x \in \Omega
\end{aligned} \tag{B.7}$$

Heat exchange

$$\begin{aligned}
&\lambda_{eff}^\sigma \nabla_y T^\sigma \cdot \boldsymbol{n} = h_h^\sigma \left[T^\sigma(t,x,y) - T^\gamma(t,x)\right] \quad y \in \partial V^\sigma(x), \ x \in \Omega \\
&Q_h(t,x) = \frac{1}{|V|} \int_{\partial V^\sigma(x)} \lambda_{eff}^\sigma \nabla_y T^\sigma \cdot \boldsymbol{n} \, dS \quad x \in \Omega
\end{aligned} \tag{B.8}$$

Air exchange

$$\begin{aligned}
&P^\gamma(t,x) = P^\sigma(t,x,y) \quad y \in \partial V^\sigma(x), \ x \in \Omega \\
&Q_a(t,x) = \frac{1}{|V|} \int_{V^\sigma} \frac{\partial \rho_a^\sigma}{\partial t} dV \quad x \in \Omega
\end{aligned} \tag{B.9}$$

All source terms, Q_v, Q_a and Q_h, are computed as the microscopic flux density q times A_σ, the
675 surface area of ∂V^σ. In the case of the vapor source term, this leads to the following expression:

$$Q_v(t,x) = \frac{A^\sigma}{|V|} q_v(t,x) \quad x \in \Omega \tag{B.10}$$

The geometrical factor $A^\sigma / |V|$ (m^2/m^3) involved in Equation (B.10) is the area of the exchange surface between phases σ and γ per unit of macroscopic volume.